Exceptional-point-based accelerometers with enhanced signal-to-noise ratio

Rodion Kononchuk[1], Jizhe Cai[2], Fred Ellis[1], Ramathasan Thevamaran[2], Tsampikos Kottos[1]
[1]Wave Transport in Complex Systems Lab, Department of Physics, Wesleyan University, Middletown, CT-06459, USA
[2]Department of Engineering Physics, University of Wisconsin-Madison, Madison, WI-53706, USA

Exceptional points (EP) are non-Hermitian degeneracies where both eigenvalues and their corresponding eigenvectors coalesce [1-4]. Recently, EPs have attracted attention as a means to enhance the responsivity of sensors, via the abrupt resonant detuning occurring in their proximity [5-20]. In many cases, however, the EP implementation is accompanied by noise enhancement leading to the degradation of sensor's performance [15-20]. The excess noise can be of fundamental nature (due to the eigenbasis collapse) or of technical nature associated with the amplification mechanisms utilized for the realization of EPs. Here we show, using an EP-based $\mathcal{PT}$-symmetric [21,22] electromechanical accelerometer, that the enhanced technical noise can be surpassed by the enhanced responsivity to applied accelerations. The noise due to eigenbasis collapse is mitigated by exploiting the detuning from a transmission peak degeneracy (TPD) – which forms when the sensor is weakly coupled to transmission lines – as a sensitivity measurant. These TPDs occur at a frequency and controlled parameters for which the bi-orthogonal eigen-basis is still complete and are distinct from the EPs of the $\mathcal{PT}$-sensor. Our device demonstrates a three-fold signal-to-noise ratio enhancement compared to configurations for which the system operates away from the TPD.

In the proximity of an N −th order EP, the degenerate resonances of an open (non-Hermitian) system abide to Puiseux generalized expansions leading to a sublinear resonance detuning $\Delta f \equiv |f - f_{EP}| \sim \varepsilon^{1/N}$ with respect to the perturbation strength ε imposed to the system by the presence of a perturbing agent. Obviously, in the small perturbation limit this sublinear response signifies an enhanced sensing as compared to a linear response, i.e. $\Delta f \sim \varepsilon \ll \varepsilon^{1/N}$, utilized by many sensing schemes that rely on Hermitian degeneracies [23-26]. In fact, the proposed EP-based protocols have additional advantages compared to other sensor schemes (e.g. slow light) whose operational principle relies on abrupt intensity variations of the measured signal. These types of sensors turned out to be extremely sensitive at the expense of their dynamic range [27,28] i.e. the ratio between the maximum and the minimum perturbation that a sensor can measure.

While increased sensor responsivity has been demonstrated in several EP-based sensors [6-10,12,17], the signal-to-noise performance has been controversially debated in recent theoretical studies [13-16,19,20]. Obviously, it is imperative to confront these disagreements via a direct experimental investigation of the effects of noise in EP-sensor performance and identify platforms and conditions (if any) under which they demonstrate superior performance. Currently, the only experiment that has analyzed the effects of noise in the EP-sensitivity (precision of a sensor) has utilized a Brillouin ring laser gyroscope platform [17,18]. Unfortunately, the conclusions of this study were discouraging as far as the performance of EP-sensing is concerned: the expected boost in responsivity of the gyroscope turned out to be limited by a broadening of the two laser linewidths due to enhanced noise effects associated with the collapse of the eigenmodes.

Here, we show experimentally and theoretically a ten-fold enhancement in responsivity to small perturbations and a three-fold signal-to-noise ratio (SNR) improvement in the sensing performance of an EP-based $\mathcal{PT}$-symmetric electro-mechanical accelerometer (see Fig. 1a). Our measuring protocol differs from the previous cases which were analyzing the lasing modes detuning of a system in the proximity to an EP. Instead, ours relies on a distinction between EPs and the transmission peak degeneracies (TPD) observed in the transmission spectrum of the $\mathcal{PT}$-symmetric sensor when it is interrogated via weakly coupled transmission lines (TL). This fact has been already recognized in a previous theoretical work [29] for the analogous concept of transmission dips. We point out that in the absence of loss/gain, these transmission dips (or peaks in our case) and their associated degenerate point are related to the newly established concept of reflectionless scattering modes (RSM) which might exhibit an EP degeneracy [30,31]. Nevertheless, the transmission dips (peaks) and their associated TPD in the case of $\mathcal{PT}$-symmetric systems are not directly related to the RSM exceptional points.

The transmission peaks frequency detuning from the TPD is influenced by the underlying EP and follows a square-root behavior with respect to the applied acceleration a. Furthermore, at TPD, the eigenbasis is still complete; thus, the performance of the sensor is not influenced by excess noise effects that might be rooted to the eigenbasis collapse. The latter has been related, in the platform of Ref. [18], with the so-called Petermann factor (PF) which diverges in the proximity of an EP, while at TPD it remains finite and smaller than the sensitivity enhancement factor SEF (compare blue and green lines in Fig. 1b) which measures the responsivity of the system to acceleration variations (see Supplementary Material). Our theoretical analysis indicates that PF is directly proportional to the technical noise due to the coupling with the TL and the noise generated by the gain/loss elements used to create the EP-singularity. The corresponding noise enhancement factors NEF^{TL}, NEF^{PT}, describing the noise power enhancements (see Supplementary Material), remain finite in the proximity of the TPD and are surpassed by the SEF of the transmission peaks detuning near the TPD (see brown and red lines in Fig. 1b).

Experimental setup - The sensor consists of a pair of capacitively coupled parity-time ($\mathcal{PT}$) symmetric RLC resonators [21] with natural frequency $f_0 = \frac{1}{2\pi}\frac{1}{\sqrt{LC}} \approx 2.68MHz$ and capacitive coupling C_c. One capacitor plate of the coupling capacitor is connected to a test-mass m which is supported by a spring attached to the platform (see Fig. 1c and Methods) and its displacement from an initial equilibrium position is used for sensing acceleration variations. The $\mathcal{PT}$-symmetry condition is achieved when the gain ($-R$), implemented using an amplifier, and loss (R) parameters are balanced, and the reactive components, L and C, satisfy mirror symmetry [21]. When the capacitive coupling is above a critical value C_c^{EP}, the system is in the so-called exact phase where the normal modes are also eigenvectors of the $\mathcal{PT}$-symmetric operator and the two eigenfrequencies are real-valued. In the opposite limit (small coupling) the system is in the broken phase where the normal modes are no longer eigenmodes of the $\mathcal{PT}$-symmetric operator while the eigenfrequencies are complex conjugates. The two phases are separated by an EP degeneracy of order $N = 2$ [22].

We have *weakly* coupled each RLC resonator to $Z = 50$ Ohm TLs via capacitors C_e. In the density plot shown in Fig. 2a, we report the measured (normalized) transmittance spectrum $T(f; a)$ versus the applied differential in-plane acceleration a. At $a = 0$ the transmission spectrum demonstrates a transmission peak degeneracy (TPD) which reflects the nearby EP degeneracy of the eigenfrequencies of the isolated system (corresponding to $C_e = 0$). The system is initially set

at TPD conditions with the coupling capacitor plates being at a distance $d \approx 20\mu m$ from one another corresponding to $C_c^{TPD} \approx 50pF$. An applied differential in-plane acceleration a displace the test-mass to a new equilibrium position, leading to a capacitive coupling detuning from C_c^{TPD} and the concomitant formation of two equi-height transmittance peaks which bifurcate from the TPD following a characteristic square-root behavior, see dashed green lines in Fig. 2a and Eq. (1) below. The weak coupling with the TLs, together with the active nature of our platform is reflected in the high intensity value of the transmittance peaks and in the narrow form of the linewidths (confined dark red area). These attributes enhance the readout and boost the sensing resolution, allowing us to identify the trajectories of the transmission peaks. Finally, the highlighted gray area indicates the displacement values of the capacitor plates for which saturable nonlinearities are triggered.

Sensitivity Analysis - Using a Coupled Mode Theory (CMT) (see Methods and Supplementary Material), we derived a scattering matrix S that models the physical system and evaluated the transmittance spectrum $T(f;a) = |S_{21}|^2$. A comparison of the measurements (Fig. 2a) with the CMT results (Fig. 2b) allowed us to extract the parameter $\gamma_e \equiv Z\sqrt{\frac{C}{L}}\left(\frac{C_e}{C}\right)^2 f_0 = 0.0206MHz$ that model the coupling of the circuit to the TLs and the gain/loss parameter $\gamma_0 \equiv R^{-1}\sqrt{\frac{L}{C}}f_0$=0.16MHz describing the amplifier/resistor used in the $\mathcal{PT}$-symmetric circuit. The CMT predictions for the frequencies $f_\pm(\epsilon)$ of the transmittance peaks (green dashed lines in Figs. 2a,b) are

$$f_\pm(\epsilon) = \begin{cases} f_0 - \epsilon \pm \sqrt{2\gamma_0\epsilon + \epsilon^2 - \gamma_e^2}, \text{ for } \epsilon \geq \epsilon_{TPD}; \\ f_0 - \epsilon, \text{ for } \epsilon \leq \epsilon_{TPD} \end{cases} \qquad (1)$$

where the CMT parameter $\epsilon = \epsilon_{TPD} + 0.0082[MHz/g] \cdot a$ models the coupling detuning due to acceleration and $\epsilon_{TPD} = -\gamma_0 + \sqrt{\gamma_0^2 + \gamma_e^2} \neq \epsilon_{EP} = 0$. Instead, we have that $\epsilon_{TPD} \approx \frac{\gamma_e^2}{2\gamma_0} \xrightarrow[\gamma_e \to 0]{} \epsilon_{EP} = 0$ as expected. Accordingly, the TPD frequency is $f_{TPD} \equiv f(\epsilon = \epsilon_{TPD}) = f_- = f_+ = f_0 - \epsilon_{TPD} \xrightarrow[\gamma_e \to 0]{} f_{EP} = f_0$. Near ϵ_{TPD}, the transmission peak frequencies Eq. (1) scale as

$$f_\pm \propto f_{TPD} \pm \sqrt{2}\sqrt[4]{\gamma_0^2 + \gamma_e^2} \cdot \sqrt{\delta\epsilon}; \text{ provided that } \delta\epsilon \ll 2\sqrt{\gamma_0^2 + \gamma_e^2}; \qquad (2)$$

where $\delta\epsilon \equiv \epsilon - \epsilon_{TPD}$. The square-root transmission peak frequency splitting Eq. (2) reflects the EP degeneracy of the eigenfrequencies $f_\pm^{(0)}(\epsilon = 0) = f_{EP} = f_0$ of the isolated system (e.g. $\gamma_e = 0$) whose functional dependence on ϵ is given by Eqs. (1,2) by substituting $\gamma_e = 0$. The presence of γ_e results in a slight enhancement of the detuning rate of $f_\pm$ as compared to the detuning rate of the resonant modes $f_\pm^{(0)}$ (blue lines in Figs. 2a,b).

The resolvability of the transmission peaks is bounded by their linewidth Γ (see Methods). The CMT predictions for the linewidth $\Gamma(\epsilon)$ are shown in the lower subfigure Fig. 2c together with the measurements which have been evaluated as the half-width at half-maximum at the transmission peak. Although $\Gamma(\epsilon)$ remains essentially constant $\Gamma(\epsilon) \approx \gamma_e$ at the parameter range where our experiment is operating, we can identify a slight increase at the proximity of ϵ_{TPD} where $\Gamma(\epsilon = \epsilon_{TPD}) = \sqrt{2}\gamma_e$ indicating that the coupling of the circuit with the leads dictates the minimum

measured uncertainty. We conclude that the uncertainty in the frequency splitting measurements in the proximity of the TPD is only slightly enhanced due to the linewidth increase [32].

The measurement of an individual frequency shift is the most common sensing scheme for (micro)electromechanical sensors [33-35]. However, a considerable advantage is obtained by measuring the frequency splitting since it is intrinsically self-referenced i.e., there is no need for an external reference to suppress or eliminate frequency drift associated with other sources. From Eq. (2) we have that $\Delta f \equiv f_+ - f_- \propto \sqrt{\delta\epsilon}$, see Fig. 2d. In case of weak coupling to the TLs the upper limit of the sublinear sensing is predominantly controlled by γ_0, see Eq. (2), while the extent of the sublinear domain is bounded by nonlinear capacitance effects occurring at small distances between the plates of the capacitor. Even with these limitations, our platform demonstrates an order of magnitude enhancement of dynamic range, as compared to conventional linear sensors with the same upper bound of dynamical range (see red double-side arrow in the inset of Fig. 2d). To further quantify the efficiency of our proposed accelerometer, we have introduced the sensitivity $\chi = \partial(\Delta f/f_0)/\partial a$ which in the proximity of the TPD demonstrates an $\sim 1/\sqrt{a}$ divergence, see Fig. 2e. A comparison with the conventional linear sensor reveals a one-order sensitivity improvement (red double-arrow).

Noise Analysis - Enhanced frequency splitting is an important aspect of efficient sensing as it guarantees an enhanced transduction coefficient from the input quantity of interest (e.g., the differential acceleration) to the output quantity (e.g., Δf). Another aspect of an efficient sensing is the precision of the measurement, which is dictated by the noise of the sensor output, and it is associated with the smallest measurable change of the input quantity. A cumulative quantification of the noise effects on the measured frequency splitting Δf, is obtained by the Allan deviation [36,37] $\sigma_{\Delta f}$ for various values of applied differential in-plane acceleration a (see Methods). The Allan deviation describes the stability of the sensor as a function of the sampling time τ. We find that $\sigma_{\Delta f}$, increases as the applied acceleration a approaches zero, i.e., in the domain where the transmission peak splitting has a square-root response. In contrast, at the domain where the frequency splitting exhibits a linear sensitivity ($a \geq 0.5\ g$) the Allan deviation $\sigma_{\Delta f}$ remains almost unchanged (compare dark blue solid line and magenta dash line in Fig. 3a). Such behavior indicates that the noise is enhanced at the vicinity of $a = 0\ g$ (where $\epsilon = \epsilon_{TPD}$) (see red arrow in Fig. 3a).

A more appropriate characterization of sensor's performance requires the analysis of the normalized Allan Deviation $\sigma_\alpha = \sigma_{\Delta f}/\chi$. Such analysis provides an estimate of the total noise effect on the measured acceleration. Of particular interest is its short-time behavior which exhibits velocity random walk behavior $\sigma_{VRW}(\tau) = \alpha_{NEA} \cdot \tau^{-1/2}$. We have found that the noise-equivalent acceleration (NEA) α_{NEA} decreases from $\alpha_{NEA} = 0.0027g \cdot Hz^{-1/2}$ at $a = 1.66g$ to a limiting value $\alpha_{NEA} = 0.00086g \cdot\ Hz^{-1/2}$, at $a = 0.01g$, see Fig. 3b, indicate that there is a three-fold signal-to-noise-ratio (SNR) improvement at the vicinity of TPD.

The α_{NEA} can be further expressed as a sum of various terms associated with different noise sources that might affect the precision of the measurements. Specifically, we have:

$$\alpha_{NEA}^2(\epsilon) \equiv \alpha_{th}^2 + \alpha_{TL}^2 + \alpha_{\mathcal{PT}}^2 + \alpha_{add}^2, \qquad \left[\text{units of } g \cdot Hz^{-\frac{1}{2}}\right]. \qquad (3)$$

The *thermal noise equivalent acceleration* α_{th} arises from a thermal Brownian motion of the test-mass. Its reduction is fundamental in minimizing α_{NEA} towards its standard quantum limit corresponding to the position uncertainty in the quantum ground state of the mechanical mass. Typically, it is overrun by the other terms in Eq. (3): the thermal noise of the TLs (α_{TL}); the $\mathcal{PT}$-

circuit noise ($\alpha_{\mathcal{PT}}$) produced by the gain-loss elements of the platform; and the added noise (α_{add}) associated with the fluctuations due to the Brownian motion of the plates of the coupling capacitors C_{c2} and C_v and the thermal noise produced from the movement of various mechanical parts of the experimental setup. Both α_{th} and α_{add} are not associated with parameters of the $\mathcal{PT}$-symmetric circuit itself and thus, do not depend on ϵ (see Methods and Supplementary Materials).

One can further understand the demonstrated sensing efficiency by realizing that $\alpha_{\mathcal{PT}} \equiv \tilde{\sigma}_{\mathcal{PT}}/\chi$ and $\alpha_{TL} \equiv \tilde{\sigma}_{TL}/\chi$ ($\tilde{\sigma}_{\mathcal{PT}}$ and $\tilde{\sigma}_{TL}$ are the spectral densities of variances in the acceleration measurements due to noise sources associated with the amplification/attenuation elements of the isolated circuit and with the TLs respectively). These spectral densities are proportional to the linewidth Γ and to the noise enhancement factors associated with the corresponding noise sources while they are inverse proportional to the transmitted signal through the electronic circuit (see Supplementary Material). The theoretical analysis based on CMT indicates that both $\tilde{\sigma}_{\mathcal{PT}}$ and $\tilde{\sigma}_{TL}$ do not experience strong variations with respect to ϵ and both saturate to a finite value at $\epsilon = \epsilon_{TPD}$. Since χ diverges at ϵ_{TPD} (green line in Fig. 1b), the NEA will decrease as $\epsilon \to \epsilon_{TPD}$ towards its noise floor level $\alpha_{NEA}^2(\epsilon \to \epsilon_{TP}) \to \ \alpha_{th}^2 \ + \alpha_{add}^2$. To appreciate further the enhancement of SNR in the proximity of the ϵ_{TPD} we have normalized NEA with respect to its value at large accelerations e.g. $a = 0.8g$. The normalized data (black circles) are shown in Fig. 3c and demonstrate a three-fold noise reduction in the proximity of TPD. The CMT results are indicated in Fig. 3c with a black solid line. Furthermore, the CMT analysis shows that the noise associated with the TL coupling and gain/loss elements used to create the sensor singularity are equivalent to voltage (or current) noise sources in the circuit. These are physically distinct from the parametrically coupled signal transduction sensing mechanism, and are transformed differently by the transmission singularity, toward a favorable SNR.

We conclude that in the specific case of accelerometers the lower limit of NEA is dictated by the Brownian motion of the test-mass and the capacitor plates which scales proportionally to the sensitivity χ. We stress that the Brownian motion has to be modeled as a fluctuation of the Hamiltonian matrix elements (i.e., coupling coefficient) while the electronic thermal noise due to amplifiers, resistors and TLs is described by additive stochastic Langevin terms in the Hamiltonian matrix. The electronic thermal noise does not scale with χ; it rather abides to a noise-specific transfer function which in the case of the $\mathcal{PT}$-symmetric circuit is proportional to the PF. Therefore, whenever the sensitivity χ overwhelms the noise-specific transfer function, the limiting value of α_{NEA} is the same for any sensing (linear or sub-linear) scheme. An example of a linear response (LR) sensing protocol that demonstrates extreme sensitivity is associated with slow light sensors, utilizing high-Q resonant modes like the ones occurring at the band-edges of a Fiber Bragg grating (FBG) [27,28]. Such sensors rely on the abrupt intensity variations of the transmission of a CW when a perturbation (e.g., stress) modifies the effective refractive index of the FBG, thus inducing a spectral shift of the high-Q Lorentzian resonance. This enhanced sensitivity is offset by an extremely short dynamic range that these sensors demonstrate: while the large sensitivity χ leads to a reduction of the lower sensing bound by minimizing the NEA, it simultaneously lowers the upper sensing bound, which is typically limited by the maximum measured signal that the sensor can output. In contrast, the enhanced sensitivity demonstrated by the TPD sensing scheme reduces the lower sensing bound, while not affecting the upper sensing bound of the measured accelerations. Additionally, in LR sensors the high sensitivity is inversely proportional to the mechanical resonant frequency of the test-mass f_n. The value of f_n dictates the operational bandwidth of the sensor - if the frequency of the applied acceleration signal exceeds the f_n this signal will not be detected by the sensor. As a result, the high sensitivity of a LR sensor also comes

at a cost of its bandwidth. Based on these key figures of merits, the performance of our proposed TPD-based proof-of-concept accelerometer compares favorably with the available on-market on-chip accelerometers such as NXP MMA1270KEG [39]. For example, they both demonstrate an $\alpha_{NEA} = 0.00086g \cdot Hz^{-1/2}$, for a measurement range up to $(\geq\ 2)\ g$, while our prototype has a 6.5 times larger operational bandwidth.

An alternative way to reach the ultimate bound of the SNR of a LR sensor is by increasing the power of the input signal to ``infinite'' levels. This is practically challenging – if not impossible. In our case, a finite power consumption enhancement is automatically taking place when the system operates near the TPD. It is therefore imperative to also take this effect into consideration when comparing the efficiency of a sensor. This point has been recently raised in Ref. [38] which introduced an additional Figure of Merit (FOM) that takes into consideration the consumed power P used for the sensing. We express FOM in terms of α_{NEA} as $FOM = (\alpha_{NEA}^2 P)^{-1}$ and plot in Fig. 3c the rescaled FOM (with the value $FOM(a = 0.8g)$ extracted from the CMT (red solid line) and the experiment (red crosses) using the measured α_{NEA}. The analysis indicates an improved FOM of the $\mathcal{PT}$-symmetric sensor in the proximity of TPD.

Conclusions - We have studied the sensing performance of a $\mathcal{PT}$-symmetric electromechanical accelerometer at the proximity to a *transmission peak degeneracy* (TPD) influenced by the presence of an underlying EP in the resonant spectrum. The TPDs occur at distinct parameter values from the EP, ensuring a completeness of the eigenbasis. At the vicinity of TPDs, we measured a three-fold SNR enhancement. Our TPD measurant protocol shows promise for the use of EP-based platforms for enhanced avionic sensors, microfluid flow sensors, pressure sensors, magnetometers, etc. Exciting future research directions include the ramifications of nonlinearities in EP-sensing performance, or the identification of physical platforms and measurant protocols where the various platform-dependent noise sources scale in such a way that the SNR is not overruled by noise.

References

[1] Kato, T. Perturbation Theory for Linear Operators, (Springer 2013)

[2] Berry, M. V. *Physics of Nonhermitian Degeneracies*, Czechoslovak Journal of Phys. 54, 1039 (2004).

[3] Miri, M.-A., Alu, A. *Exceptional Points in Optics and Photonics*, Science 363, eaar7709 (2019).

[4] Parto, M., Liu, Y. G. N., Bahari, B., Khajavikhan, M. & Christodoulides, D. N. *Non-Hermitian and topological photonics: optics at an exceptional point*, Nanophotonics 10, 403 (2021).

[5] Wiersig, J. *Enhancing the sensitivity of frequency and energy splitting detection by using exceptional points: application to microcavity sensors for single-particle detection*, Phys. Rev. Lett 112, 203901 (2014).

[6] Hodaei, H., Hassan, A. U., Wittek, S., Garcia-Gracia, H., El-Ganainy, R., Christodoulides, D. N. & Khajavikhan, M. *Enhanced sensitivity at higher-order exceptional points*, Nature 548, 187 (2017)

[7] Chen, W., Ozdemir, S. K., Zhao, G., Wiersig, J. & Yang, L. *Exceptional points enhance sensing in an optical microcavity*, Nature 548, 192 (2017).

[8] Chen, P-Y, Sakhdari, M., Hajizadegan, M., Cui, Q., Cheng, M. M.-C., El-Ganainy, R., & Alú, A. *Generalized parity-time symmetry condition for enhanced sensor telemetry*, Nature Electronics 1, 297 (2018).

[9] Dong, Z., Li, Z., Yang, F., Qiu, C.-W. & Ho, J. S. *Sensitive readout of implantable microsensors using a wireless system locked to an exceptional point*, Nature Electronics 2, 335 (2019).

[10] Hokmabadi, M. P., Schumer, A, Christodoulides, D. N. & Khajavikhan, M. *Non-Hermitian ring laser gyroscopes with enhanced Sagnac sensitivity*, Nature 576, 70 (2019).

[11] Kononchuk, R. & Kottos, T. *Orientation-sensed optomechanical acelerometers based on exceptional points*, Phys. Rev. Research 2, 023252 (2020).

[12] Park, J.-H., Ndao, A., Cai, W., Hsu, L., Kodigala, A., Lepetit, Th., Lo, Y.-H. & Kanté, B. *Symmetry-breaking-induced plasmonic exceptional points and nanoscale sensing*, Nature Physics 16, 462 (2020).

[13] Xiao, Z., Li, H., Kottos, T., & Alú, A. *Enhanced Sensing and Nondegrated Thermal Noise Performance Based on $\mathcal{PT}$-Symmetric Electronic Circuits with a Sixth-Order Exceptional Point*, Phys. Rev. Lett. 123, 213901 (2019).

[14] Zhang, M., Sweeney, W., Hsu, C.-H., Yang, L., Stone, A. D., & Jiang, L. *Quantum Noise Theory of Exceptional Point Amplifying Sensors*, Phys. Rev. Lett. 123, 180501 (2019).

[15] Lau, H.-K. & Clerk, A. A. *Fundamental limits and non-reciprocal approaches in non-Hermitian quantum sensing*, Nat. Comm. 9, 4320 (2018).

[16] Wiersig, J. *Prospects and fundamental limits in exceptional point-based sensing*, Nature Comm. 11, 2454 (2020).

[17] Lai, Y.-H., Lu, Y.-K., Suh, M.-G., Yuan, Z., & Vahala, K. *Observation of the exceptional-point-enhanced Sagnac effect*, Nature 576, 65 (2019).

[18] Wang, H., Lai, Y.-H., Yuan, Z., Suh, M.-G. & Vahala, K. *Petermann-factor sensitivity limit near an exceptional point in a Brillouin ring laser gyroscope*, Nat. Comm. 11, 1610 (2020).

[19] Langbein, W. *No exceptional precision of exceptional-point sensors*, Phys. Rev. A 98, 023805 (2018).

[20] Wiersig, J. *Robustness of exceptional point-based sensors against parametric noise: The role of Hamiltonian and Liouvillian degeneracies*, Phys. Rev. A 101, 053846 (2020).

[21] JSchindler, J., Lin Z., Lee, J. M., Ramezani, H., Ellis, F. M., & Kottos, T. *$\mathcal{PT}$-symmetric electronics*, J. Phys. A- Math. Theor. 45, 444029 (2012).

[22] Bender, C. M. & Böttcher S. *Real spectra in non-Hermitian Hamiltonians having $\mathcal{PT}$-symmetry*, Phys. Rev. Lett. 80, 5243 (1998).

[23] Fraden, J. *Physical Principles of Sensing. In: Handbook of Modern Sensors*, Springer, Cham. (2016)

[24] Xiao, G. & Bock, W. J. *Photonic Sensing: Principles and Applications for Safety and Security Monitoring*, Wiley Series in Microwave and Optical Engineering, (2012).

[25] Bao, M. *Micro mechanical transducers: pressure sensors, accelerometers and gyroscopes*, (Elsevier, 2000).

[26] De Brito Andre, P. S. & Humberto, V. *Accelerometers: Principles, Structure and Applications*, (Nova Science Publishers, 2013).

[27] Wen, H., Skolianos, H. G., Fan, S., Bernier, M., Vallée, R. & Digonnet, M. J. *Slow-Light Fiber-Bragg-Grating Strain Sensor With a 280-femtostrain/$\sqrt{Hz}$} Resolution,* J. Light. Technol 31 11 (2013).

[28] G. Skolianos, A. Aurora, M Bernier, M. J.Digonnet, *Slow light in Bragg gratings and its applications*, J. Phys. D: Appl. Phys. 49, 463001 (2016).

[29] Geng, Q., Zhu, K.-D. *Discrepancy between transmission spectrum splitting and eigenvalue splitting: a reexamination on exceptional point-based sensors*, Photon. Res. 9 1645-1649 (2021).

[30] Sweeney, W. R., Hsu, C. W., Rotter, S. & Stone, A. D. *Perfectly Absorbing Exceptional Points and Chiral Absorbers*, Phys. Rev. Lett. 122, 093901 (2019).

[31] Sweeney, W. R., Hsu, C. W. & Stone, A. D. *Theory of reflectionless scattering modes*, Phys. Rev. A 102, 063511 (2020).

[32] Yoo, G., Sim, H.-S. & Schomerus, H. *Quantum noise and mode nonorthogonality in non-Hermitian $\mathcal{PT}$-symmetric optical resonators*, Phys. Rev. A 84, 063833 (2011).

[33] Krause, A. G., Winger, M.T., Blasius, D., Lin, Q. & Painter, O., *A microchip optomechanical accelerometer*, Nat. Photonics 6, 768 (2012).

[34] Li, Y. L. & Barker, P. F. *Characterization and Testing of a Micro-g Whispering Gallery Mode Optomechanical Accelerometer*, J. Light. Technol. 36, 3919 (2018).

[35] Regal, C. A., Teufel, J. D. & Lehnert, K. W. *Measuring nanomechanical motion with a microwave cavity interferometer*, Nat. Physics 4, 555 (2008).

[36] El-Sheimy, N., Hou, H. & Niu, X., *Analysis and Modeling of Inertial Sensors Using Allan Variance*, IEEE Transactions on Instrumentation and measurement 57, 140 (2008).

[37] Quinchia, A. G., Falco, G., Falletti, E., Dovis, F. & Ferrer, C. *A comparison between different error modeling of MEMS applied to GPS/INS integrated systems*, Sensors 13, 9549 (2013).

[38] Duggen, R., Mann, S. & Alú, A. *Limitations of Sensing at an Exceptional Point*, submitted (2021).

[39] https://www.nxp.com/docs/en/data-sheet/MMA1270KEG.pdf.

Acknowledgments: We acknowledge partial support from NSF-CMMI-1925543, NSF-CMMI-1925530, ONR N00014-19-1-2480 and from a grant from Simons Foundation for Collaboration in MPS No. 733698. RT and JC also acknowledge the partial support for this research provided by the University of Wisconsin-Madison, Office of the Vice Chancellor for Research and Graduate Education with funding from the Wisconsin Alumni Research Foundation.

Author contributions: R.K., J.C., F. E. and R.T. designed the mechanical device. R.K. and F. E. designed and fabricated the electronic circuit. J.C. and R.T. fabricated the mechanical device. R.K. performed the characterization and data processing of the accelerometer and developed the theory with the support of T.K. All authors discussed the results. T.K. conceived the project. R.K. and T.K. wrote the manuscript with input from all authors.

Competing interests: The authors declare that they have no competing interests.

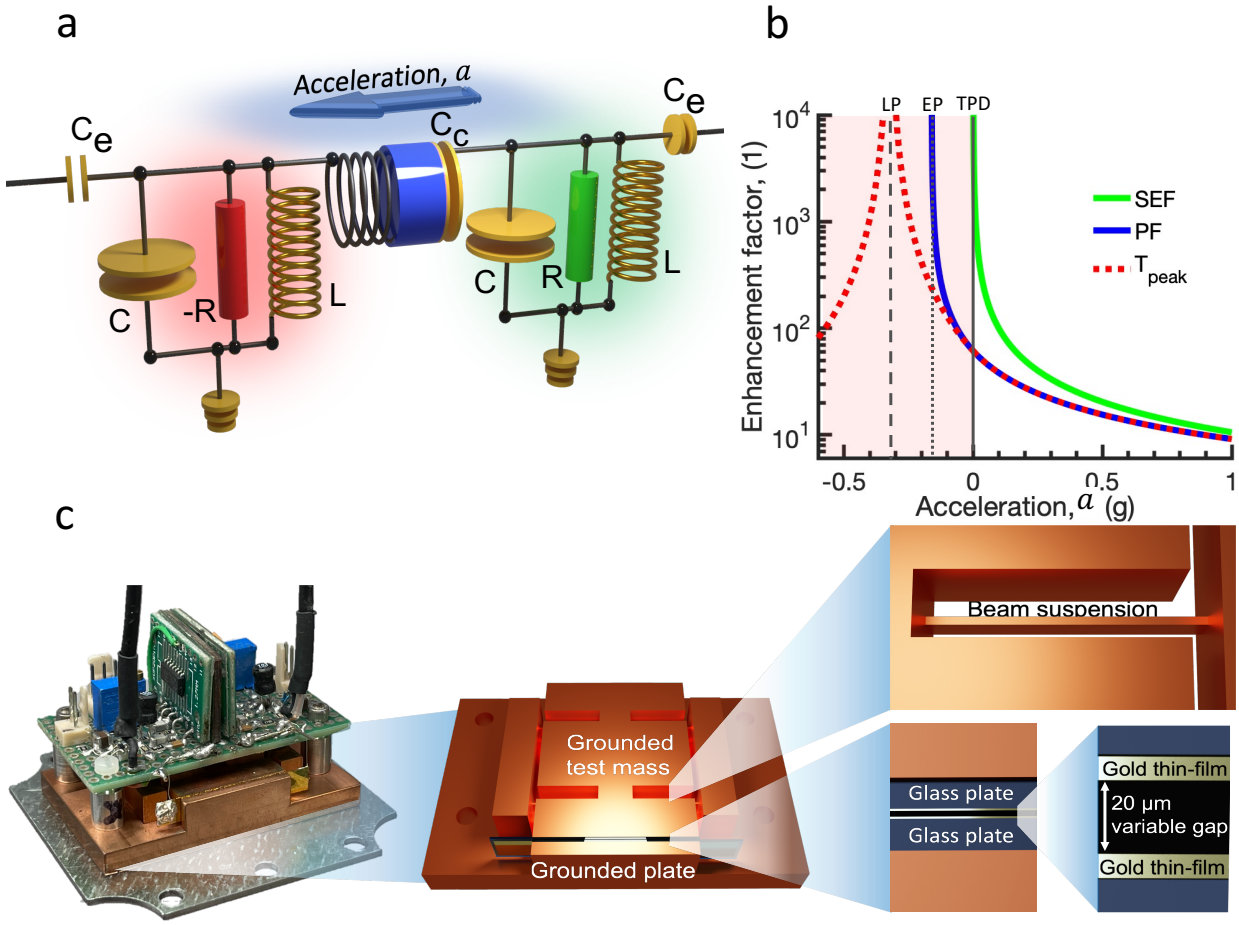

Figure 1: **$\mathcal{PT}$-symmetric platform for enhanced acceleration sensing. a,** Schematic of the $\mathcal{PT}$-symmetric electromechanical sensor. The $\mathcal{PT}$-symmetric circuit is capacitively coupled to the transmission lines with a capacitor C_e. The two circuit tanks are coupled together with a variable capacitor C_c with one plate connected to a test mass that senses the acceleration. **b,** The behavior of the sensitivity enhancement factor SEF (green line), Petermann factor PF (blue line), and of noise enhancement factors associated with the $\mathcal{PT}$-symmetric components of the circuit $NEF^{\mathcal{PT}}$ (dark red dotted line) and the transmission line NEF^{TL} as a function of the applied acceleration a (magenta dotted line). The black vertical lines indicate the TPD (solid), EP (dotted) and LP (dashed) points. The highlighted domain indicates the accelerations which are not captured by the experimental platform. **c,** The actual acceleration sensing platform utilizes a micro-fabricated coupling capacitor which is connected to the test-mass used to sense the applied acceleration.

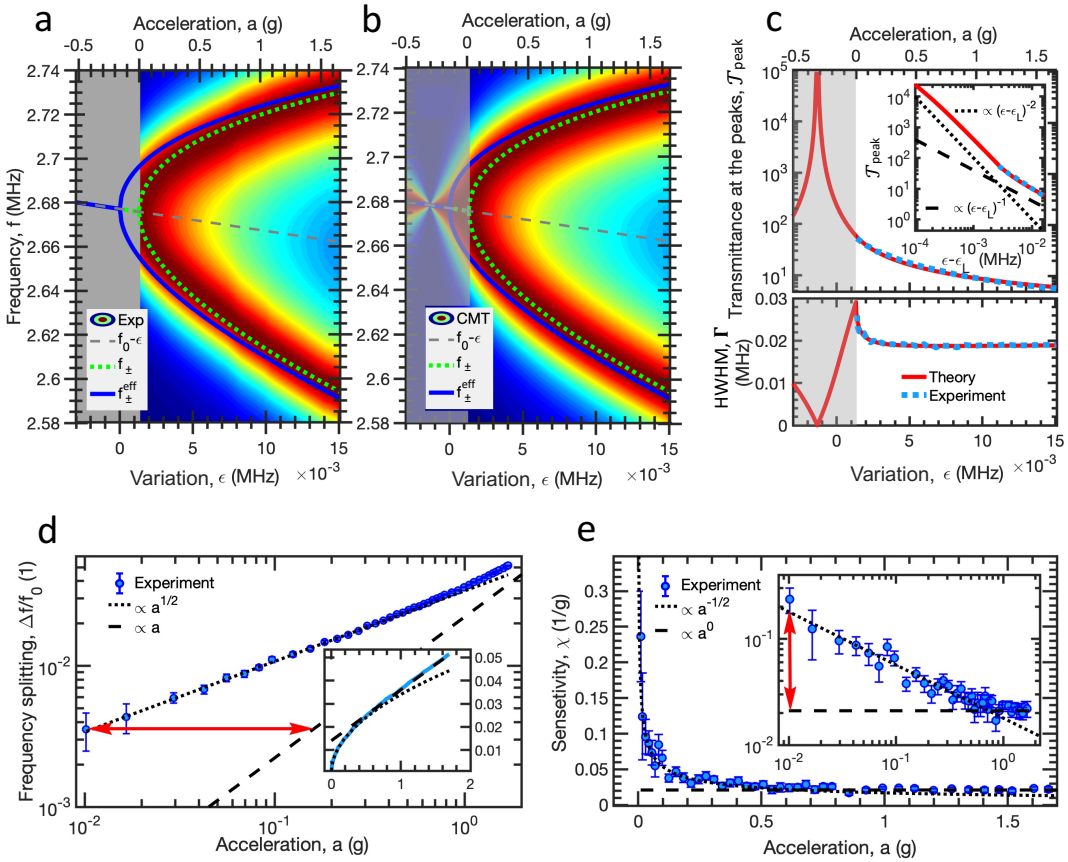

Figure 2: **Experimentally measured response of the sensor to applied acceleration**. **a,** Density plot of the measured normalized transmittance spectrum versus acceleration a (top x-axis). The bottom x-axis indicates the associated capacitance variation $\epsilon(a)$. The trajectory of the transmittance peaks is indicated with green dashed lines. At the proximity of the TPD the peaks demonstrate a square-root behavior, see Eqs.(1,2). The trajectories of the eigenfrequencies of the isolated dimer are shown by dark blue lines. They coalesce at $\epsilon = 0$ (EP degeneracy). The highlighted gray area is excluded from our measurements. In this domain, saturable nonlinearities are triggered. **b,** The same as in **a** for the transmittance spectrum calculated using a CMT. **c,** (Top) The transmission peak versus the capacitance variation $\epsilon(a)$. The red line indicates the CMT predictions while the dotted light blue line is the measured data. The inset presents the same data in a double-logarithmic fashion referring to the capacitance variations with respect to the lasing point. The dashed and dotted black lines indicate a logarithmic slope of -1 and -2. (Bottom) The behavior of half-width-half-maximum linewidth Γ versus ϵ in the proximity of the TPD. The red (dotted light blue) line indicates the CMT (experimental) results. **d,** The measured relative transmission peak splitting $\Delta f/f_0$ versus the applied differential acceleration a plotted in double-logarithmic plot. The dotted (dashed) black line indicates a square-root (linear) scaling with a. Inset shows the same data in linear plot. The red arrow shows the dynamical range enhancement of the proposed accelerometer with respect to an equivalent sensor based on linear response. **e,** The sensitivity of the $\mathcal{PT}$-symmetric accelerometer demonstrating an order (red arrow) enhancement in the proximity of the EP as opposed to a system configuration away from the EP. In the inset we report the same data in a double-logarithmic plot. Error bars on panels **d** and **e** denote ± 1 standard deviation obtained from 10 independent measurements.

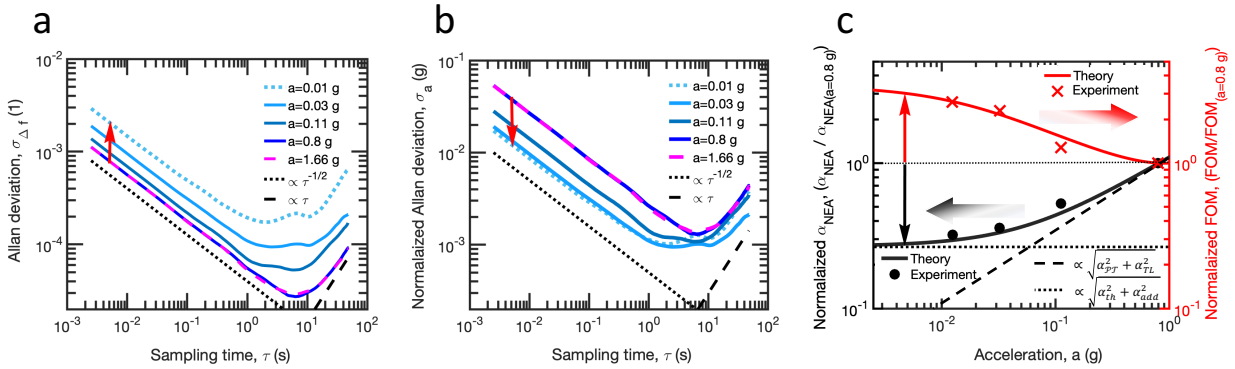

Figure 3: **Measured Allan Deviation. a,** Measured Allan deviation $\sigma_{\Delta f}$ of the transmission peaks splitting as a function of the sampling time τ for various values of the applied acceleration a (see legend). The enhancement of $\sigma_{\Delta f}$ at the vicinity of the TPD at $a = 0$ g is shown by red arrow. **b,** Measured normalized Allan deviation $\sigma_\alpha = \sigma_{\Delta f}/\chi$ as a function of the sampling time τ for various values of the applied acceleration a (see legend). The suppression of σ_α due to enhanced sensitivity at the vicinity of $a = 0$ g is shown by red arrow. The black dotted lines on panels (**a,b**) indicate a power decay $\tau^{-1/2}$, associated with a VRW regime, while the black dashed lines are proportional to τ indicating the presence of a RR regime. **c,** The normalized noise equivalent acceleration $\alpha_{NEA}/\alpha_{NEA}(a = 0.8\text{g})$ (black line and circles and the normalized $FOM/FOM(a = 0.8\text{g})$ (red line and crosses) versus the applied differential acceleration. The black/red arrows indicate a threefold reduction/enhancement of the noise/FOM in the proximity of the TPD. The black dashed line describes the contribution to α_{NEA} associated with the internal and the external noise sources $\sqrt{(\alpha_{\mathcal{PT}}^2 + \alpha_{TL}^2)}$, while the contribution associated with the thermal noise and the added noise $\sqrt{(\alpha_{th}^2 + \alpha_{add}^2)}$ is shown by a black dotted line. Both terms are normalized with $\alpha_{NEA}(a = 0.8\text{g})$.

Methods

Transmittance spectrum and frequency splitting measurements - The transmitted signal through the electronic circuit was collected for different applied in-plane projections of gravity acceleration. The device was mounted on a rotational stage Newport ESP100BCC which was electronically controlled via a Newport ESP301 controller. The setup allows to control the horizontal tilt of the device with minimal increment of 0.2 mdeg and, thus, vary the in-plane projection of the gravity acceleration in a range of 2g ([-1 g :1 g]). At each specific tilting angle the transmission spectrum was collected using an ENA network analyzer Keysight E5080A. The individual frequency sweeps contain 401 points in a range of 2.58 MHz - 2.74 MHz, with intermediate frequency bandwidth of 1.5 MHz. Single measurement is obtained from the collected spectrum which was averaged over 100 consecutive individual sweeps for each applied acceleration, which resulted in a sampling time of $\tau \approx 25$ ms. The frequencies of the transmittance peaks $f_\pm$ were then identified from the resulted spectrum, which allows to calculate the frequency splitting Δf.

Coupled Mode Theory modeling - To better understand the outcome of these measurements we have performed a theoretical analysis using the most general framework of coupled mode theory (CMT) which was appropriately mapped to describe our $\mathcal{PT}$ -symmetric circuit (see details in the

Supplementary Material). Specifically, the scattering matrix S that describes the open circuit, takes the form

$$\boldsymbol{S}(f) = -\boldsymbol{I} - i\boldsymbol{W}\boldsymbol{G}(f)\boldsymbol{W}^{T};\ \boldsymbol{G}(f) = \left(\boldsymbol{H}_{eff} - f\,\boldsymbol{I}\right)^{-1}; \qquad (4)$$

where, $\boldsymbol{I}$ is the two-dimensional identity matrix and $\boldsymbol{G}(f)$ is the Green's function. The effective Hamiltonian $\boldsymbol{H}_{eff}$ that describes the $\mathcal{PT}$-symmetric dimer coupled to the TLs is

$$\boldsymbol{H}_{eff} = \boldsymbol{H}_0 - \frac{i}{2}\boldsymbol{W}^{\boldsymbol{T}}\boldsymbol{W};\ \boldsymbol{H_0} = \begin{pmatrix} f_0 - \epsilon + i\gamma_0 & \gamma_0 + \epsilon \\ \gamma_0 + \epsilon & f_0 - \epsilon - i\gamma_0 \end{pmatrix}; \qquad (5)$$

where the diagonal matrix $\boldsymbol{W}_{nm} = \delta_{nm}\sqrt{2\gamma_e}$ models the coupling of the dimer with the TLs and $\boldsymbol{H_0}$ is the Hamiltonian of the isolated dimer (corresponding to $\gamma_e = 0$). For $\epsilon = \epsilon_{EP} = 0$ the isolated system forms a second order ($N = 2$) EP degeneracy at frequency $f_{\pm}^{(0)} \equiv f_{EP} = f_0$ (see Supplementary Material).

Using Eq. (4) we have extracted the transmittance $T(f; a) = |S_{21}|^2$ and via direct comparison with the experimental data we were able to identify the various parameters that have been used in our CMT modeling. Specifically, we have estimated that the linewidth of the resonances of the individual circuit tank, due to its coupling with the TL is $\gamma_e \equiv Z\sqrt{\frac{C}{L}}\left(\frac{C_e}{C}\right)^2 f_0 = 0.0206\ MHz$. Similarly, we have found that the variations at the coupling strength between the two resonant modes of the dimer, due to the displacement of the plates of the capacitor C_c when an acceleration a is imposed to the system, can be modeled by the parameter $\epsilon(a) = \epsilon_{TPD} + 0.0082\left[\frac{MHz}{g}\right]\cdot a$. The coupling strength in the absence of any acceleration is $\epsilon_{TPD} = 0.0013\ MHz$ - and is associated with the TPD. Finally, $\gamma_0 = R^{-1}\sqrt{\frac{L}{C}} f_0 = 0.16\ MHz$, is the CMT gain/loss parameter describing the amplifier/resistor used in the $\mathcal{PT}$-symmetric circuit.

Lasing Threshold and Transmission peak scaling - To guarantee the stability of our system, we have also identified theoretically the lasing condition of the open circuit (see Supplementary Material). The latter is associated with the real poles of the scattering matrix Eq. (4) occurring at $f_L = f_0 - \epsilon_L$ where $\epsilon_L = -\gamma_0 + \sqrt{\gamma_0^2 - \gamma_e^2} < \epsilon_{EP} = 0 < \epsilon_{TPD}$. Its existence can be also recognized by the divergence of the transmission at this frequency and perturbation values. In the upper subfigure of Fig. 2c we report the un-normalized transmission peaks $T_{peak} = T(f_{\pm}; \epsilon)$ extracted from the measurements (dashed blue line), together with its theoretical values calculated using the CMT modeling (red line). We find that at the lasing point $T_{peak}(\epsilon \to \epsilon_L) \to \infty$ as expected. The divergence is characterized by a $T_{peak}(\epsilon) \propto (\epsilon - \epsilon_L)^{-2}$ $[T_{peak} \propto (\epsilon - \epsilon_L)^{-1}]$ scaling, which applies in the range $\epsilon < \epsilon_{TPD}$ $[\epsilon > \epsilon_{TPD}$ and it is nicely confirmed from the experimental data].

Transmission peak resolvability and Linewidth bound - While an enhanced transmitted intensity is an important element for the readability of the output signal and the identification of the transmission peak frequencies $f_{\pm}$, the other crucial factor is the sensing resolution. This bound is proportional to the linewidth Γ of the transmission peaks. In the limit of very strong coupling $\epsilon \gg \gamma_0$, we can disregard the $\mathcal{PT}$ nature of the circuit and we expect that the linewidth Γ will be dictated by the coupling of the dimer with the TLs. The latter is characterized by the coupling constant γ_e which in our setting takes the value $\gamma_e \approx 0.02, MHz$. At the other limiting case of $\epsilon \to$

ϵ_L we expect a narrowing of the linewidth which in the semiclassical picture (e.g. without taking into consideration the non-orthogonality of the modes etc) becomes zero. In fact, the CMT modeling provides us with the possibility to derive an exact expression for the linewidth $\Gamma(\epsilon)$ for the whole range of perturbations ϵ (see Supplementary Material). These CMT results are shown in the lower subfigure Fig. 2c together with the extracted values from the measurements which have been evaluated as the half-width at half-maximum (HWHM) at the transmission peak. Although $\Gamma(\epsilon)$ remains essentially constant $\Gamma(\epsilon) \approx \gamma_e$ at the parameter range where our experiment is operating, we are able to identify a slight increase in the proximity of ϵ_{TPD}. Specifically, our CMT analysis indicates that for $\delta\epsilon \equiv \epsilon - \epsilon_{TPD} \geq 0$ the linewidth takes the form $\Gamma(\delta\epsilon \to 0) \sim \sqrt{2}\gamma_e - \sqrt{2}(\gamma_e^2 + \gamma_0^2)^{1/4}\sqrt{\delta\epsilon}$. For $\delta\epsilon = 0$ we get that $\Gamma(\delta\epsilon = 0) = \sqrt{2}\gamma_e$ indicating that the coupling of the circuit with the leads dictates the minimum measured uncertainty. This prediction is confirmed by the measurements (see light blue dotted line in Fig. 2c). On the other side of ϵ_{TPD} i.e. $\delta\epsilon < 0$ the linewidth behaves as $\Gamma(\epsilon) \approx \sqrt{2}\gamma_e + \frac{\sqrt{2(\gamma_e^2+\gamma_0^2)}}{\gamma_e}\delta\epsilon$. This small $\delta\epsilon$ expansion persists even for $\epsilon \approx \epsilon_{EP}$ where $\Gamma(\epsilon = \epsilon_{EP}) \approx 0.7\gamma_e$. From this analysis we conclude that the uncertainty in the frequency splitting measurements in the proximity of the TPD is only slightly enhanced due to the linewidth increase [32]. Nevertheless, it can be always confined to small values when the system operates in the weak coupling regime. Of course, this conclusion is subject to the analysis of other characteristics like the sensitivity or other noise sources that might also affect the measurement process.

Allan deviation measurement - The Allan deviation $\sigma_{\Delta f}(\tau)$ of the transmission peak splitting is defined as

$$\sigma_{\Delta f}(\tau) = \frac{1}{2(M-1)} \sum_{n=1}^{M-1} \left(\overline{\Delta f}_{n+1} - \overline{\Delta f}_n\right)^2 ; \qquad (6)$$

where τ is the sampling time, M is the total number of frequency measurements, and $\overline{\Delta f}_n$ indicates the average frequency splitting during the sampling time interval $[n\tau, (n+1)\tau]$. For the extraction of Allan deviation the transmittance peak splittings Δf were sampled with frequency of 400 Hz ($\tau_{min} = 2.5\ ms$) over a period of 90 s.

Brownian motion contributions to noise-equivalent acceleration – The contributions to the NEA from the Brownian motion of the test-mass is given by $\alpha_{th} = \sqrt{4k_B T\ \omega_n/mQ}$. In this expression k_B is the Boltzmann's constant, $T = 293\ K$ is the ambient temperature, $m = 27$gr is the mass, $\omega_n = 2\pi\ f_n = 2513 rad/sec$ is the frequency and $Q = 40$ is the quality factor of the resonant mode of the mechanical test-mass (see below design and fabrication details of the spring-mass).

Evaluation of NEA – We have analyzed the contribution of the various noise sources to the cumulative spectral density of the variance in the frequency splitting $\sigma_{\Delta\tilde{\omega}}$. Broadly speaking, it can be decomposed into two terms: (a) $\sigma_{\Delta\tilde{\omega}}^{C}$ associated with the uncertainty in the measurement of the transmission peaks splitting $\Delta\tilde{\omega}$, due to the cumulative circuit noise generated by the gain/loss elements of the circuit and the ambient noise of the transmission lines [see Eqs. (S38,S40) in the Supplementary Material]; and (b) $\sigma_{\Delta\tilde{\omega}}^{\kappa}$ [see section S6 in the Supplementary Material] associated

with uncertainty in the measurement of the transmission peaks splitting $\Delta\tilde{\omega}$, due to the fluctuations of the coupling strength between the two RLC circuit tanks. We can now express the cumulative spectral density of the variance in terms of these quantities as $\sigma^2_{\Delta\tilde{\omega}}=\left[\left(\sigma^C_{\Delta\tilde{\omega}}\right)^2+(\sigma^{\kappa}_{\Delta\tilde{\omega}})^2\right]$. Skipping the details of the calculation (see section S7 in the Supplementary Material), the result for $\alpha^2_{NEA}(\epsilon)=\frac{1}{\chi^2(\epsilon)}\frac{\sigma^2_{\Delta\tilde{\omega}}}{\Delta_f}$ (Δ_f is inversely proportional to the sampling time over which the signal is measured and averaged) is

$$\alpha^2_{NEA}(\epsilon)\propto\left\{\frac{k_BT\Gamma^2(\epsilon)}{\left|a^{in}_{L1}\right|^2}\left(2R\frac{\gamma_0}{\gamma_e}\cdot((\gamma_0+\epsilon)^2-\gamma_0\gamma_e)+Z_0\cdot((\gamma_0+\epsilon)^2+\gamma_0^2)\right)(2\gamma_0\epsilon+\epsilon^2-\gamma_e^2)+\left(\sigma^{\kappa}_{\epsilon,add}\right)^2\right\}\left(\frac{\partial\epsilon}{\partial a}\right)^{-2}+\frac{4k_bT\omega_n}{mQ},\qquad(7)$$

where we have used the expression $\chi^2(\epsilon)=4SEF(\epsilon)\cdot\left(\frac{\partial\epsilon}{\partial a}\right)^2$ for the sensitivity of the frequency splitting between the transmission peaks with respect to an applied acceleration a. The first term in Eq. (7) describes $\alpha^2_{\mathcal{PT}}$, the second is α^2_{TL}, the third is α^2_{add} and the last term is associated with α^2_{th}, see Eq. (5). The behavior of the various noise terms that contribute to α_{NEA} and their scaling with respect to the acceleration a is reported in Fig. 3c. A more detail analysis of the expression Eq. (7) is further presented at section S7 in the Supplementary Material.

Long-time behavior of Allan deviation – We have also analyzed the long-time growth of $\sigma_\alpha(\tau)$ (see Fig. 3). This analysis allows us to extract the so-called drift rate ramp (DRR), describing systematic (deterministic) errors due to temperature fluctuations. By definition $\sigma_{DRR}(\tau)=\alpha_{DRR}\cdot\tau$, with best fit $\alpha_{DRR}\approx 0.0007\ g\cdot s^{-1}$ for almost all acceleration values. Finally, the saturation value $\sigma_{BI}(\tau)=\alpha_{BI}\cdot\tau^0$ of the Allan deviation (black dashed line) is indicative of the Bias Instability (BI), and sets the smallest possible reading of our sensor due to the random flickering of electronics or other components. The extracted value ranges from $\alpha_{BI}\approx 0.0009\,g$ (accelerations closer to TPD) to $\alpha_{BI}\approx 0.0014\,g$ (accelerations away from TPD).

Figure of Merit (FOM) and consumed power -Using the CMT analysis (see Supplementary material) one can show that:

$$|S_{21}|^2+|S_{11}|^2+2\gamma_2|a_2|^2-2\gamma_1|a_1|^2-1=0;\ \boldsymbol{a}=-i\boldsymbol{G}\boldsymbol{W}^T(1,0)^T;\qquad(7)$$

where $\gamma_1(\gamma_2)$ is the gain(loss) of the first (second) cavity. In our settings $\gamma_1=\gamma_2=\gamma_0$. The total power P consumed by the platform is

$$P=\int_{f_{min}}^{f_{max}}(|S_{21}|^2+|S_{11}|^2+2\gamma_2|a_2|^2)\left|\boldsymbol{a}^{in}_{TL_1}\right|^2df=\int_{f_{min}}^{f_{max}}(2\gamma_1|a_1|^2+1)\left|\boldsymbol{a}^{in}_{TL_1}\right|^2df.\quad(8)$$

In our experimental platform $f_{min}=2.58$ MHz and $f_{max}=2.74$ MHz, which are the lower/upper bound of frequency range used to perform the measurements. Taking into account the fact that the input signal $\boldsymbol{a}^{in}_{TL_1}$ has a uniform spectral density, the FOM introduced in Ref. [38] is written as

$$FOM = (\alpha_{NEA}^2 P)^{-1} \propto \int_{f_{min}}^{f_{max}} (\alpha_{NEA}^2(|S_{21}|^2 + |S_{11}|^2 + 2\gamma_2|a_2|^2))^{-1}\, df. \quad (9)$$

We fitted the extracted S_{21} scattering parameter with the CMT results, in order to estimate the consumed power total power P using Eq. (8). This information, in combination with the experimental data for α_{NEA}, allows us to estimate the FOM using Eq. (9).

Circuit design and fabrication-The detailed schematics of the $\mathcal{PT}$-symmetric circuit is shown in the Extended data Fig. 1. The main elements of the circuit are a pair of RLC resonators, where resistor, inductor and capacitor are connected in parallel to ground. The inductor L in each unit is a Murata 11R103C with inductance of $L = 10\ \mu H$. The total capacitance consists of a pair of in-parallel connected capacitors C and C_v, where the former one is Murata GRM21A5CE271JW01D with fixed value of $C = 270\ pF$, while the latter one is a voltage controlled capacitor Murata LXRW0YV33-0-056 with variable capacitance $C_v = 16.5 - 33\ pF$. It is used to precisely control the resonant frequency of each resonator. External voltage was used in order to control the C_v. It was applied via an EG&G 7265 DSP Lock-in amplifier, connected via a BNC port through a resistor R_v Yageo RC0402FR-75KL with resistance $R_v = 5$ kOhm and grounded $10\mu F$ capacitance C_{v1} Murata GCM32EL8EH106KA7. The total resistance in each resonator unit consists of a fixed resistor R_1 Bourns CR1206FX-1101ELF with resistance $R_1 = 1.1$ kOhm, which is connected in-series with a mechanically controlled variable resistor R_2 Bourns 3296'w-1-20RLF with resistance $R_2 = 0 - 200$ Ohm.

In the first resonator these resistors are connected to the output voltage port of an operational amplifier (Op Amp) in order to produce gain. The Op Amp used in the circuit is one of the three on-chip Op Amps of the Analog Devices ADA4862-3 triple amplifier. The internal resistance between the inverting port to ground is $R_{G1} = 550$ Ohm . This is the same as the resistance between the output port and the inverting input port $R_{G2} = 550$ Ohm (see extended data Fig. 1). The non-inverting input of the amplifier unit is connected to the node of the first resonator via the resistor Rs, Bourns RC0402FR-075KL with resistance $R_s = 133$ Ohm. The second unit of the same ADA4862-3 triple amplifier is connected with non-inverting input to the node of the first resonator through the same resistance $R_s = 133$ Ohm. The resistor R_{G2} is left floating in order to obtain a unity gain. The tripple amplifier is powered via the voltage source through ports -Vs and +Vs, as shown in extended data Fig. 1. The output port of the Op Amp unit is connected with the probing input BNC port via the capacitor Ce, Murata GCM1887U1H103JA6J with capacitance $C_e = 10$ nF. This capacitance was used to block the DC-signals from entering the circuit, while the coupling of the input probing signal is achieved via parasitic capacitive coupling between the input BNC port and the circuit elements. The resistors R_{e1}, Bourns CRM1206FX2700ELF with resistance $R_{e1} = 270$ Ohm and R_{e2}, Bourns CR1206FX60R4ELF with resistance $R_{e1} = 50$ Ohm are connected as shown in the extended data Fig. 1 to match the circuit impedance with the 50 Ohm coaxial cable connected to the BNC port.

In the second resonator unit the resistors R_1 and R_2 are connected to ground in-parallel to the capacitors C and C_v. The probing output BNC port is connected to the node of the second resonator through the Op Amp unit of another ADA4862-3 triple amplifier. The Op Amp unit operates in a unity gain regime (similar to the second Op Amp connected to the node of the first resonator).

The two resonator units are capacitively coupled together using a trimmed capacitor C_{c2} Knowles JZ300HV with variable capacitance $C_{c2} = 5.5 - 30$ pF. The spring-mass is coupled to the circuit producing an extra coupling capacitance $C_{cv} \approx 35$ pF, when the spring-mass is at rest. When an in-plane acceleration is applied, the mass with the attached capacitor plate moves toward the stationary plate, resulting in an increase of the capacitance C_{cv} . The circuit was built on a prototype board and was mounted on top of the spring-mass as it is seen in Fig. 01. The electrodes of the spring mass were connected to the circuit with 0.18 mm wires which provides enough flexibility during the motion of the test-mass. The wires were glued to the electrodes using silver filled epoxy adhesive MG Chemicals 8331-14G.

Spring-mass capacitive sensor design and fabrication-The spring-mass capacitive sensor consists of two main pieces. The first one is a base plate shown in Figs. 2a and b. It consists of a 56 x 25 mm x 5 mm copper plate with one side having a 20 mm long ledge with 6 mm height. The ledge is used to mount the stationary capacitor plate. The second main piece is a 0.027 kg, 5 mm thick copper mass which is suspended on four 10 x 0.3 x 2 mm bendable beams attached to stationary stands (see Figs. 2c and d). The mass is suspended 1 mm above the bottom level of the stationary stands. The mass and base plates were micro machined using electrical discharge machining (EDM) technique. The pair of 23 x 0.5 x 5 mm glass substrates were used to sputter (PVD) a 10 nm thin Ti layer followed by a 100 nm thin Au layer which acts as electrodes for the capacitor plates. One of the glass plates was glued to the ledge of the base plate (as it is shown in Fig. 3a) at the noncoated side. In a similar manner the second plate was glued to the back vertical surface of the copper mass at the noncoated side (see Fig. 3b). The copper mass with the glass plate was then mounted on the copper base and glued with a conductive adhesive (see Fig. 3c). The assembly was performed under a microscope with a custom built micro-translational stage to achieve the $20\mu m$ gap between the two gold-metalized surfaces of the glass plates (see inset in Fig. 3c). The spacing between the pair of glass plates with gold nanolayers forms a capacitance of about 35 pF, when the mass is at rest. When an acceleration is applied to the platform, the plates are moving closer to one another, leading to an increase of the capacitance. The open parts of the metalized surfaces were connected to the circuit as it is discussed above, while the platform and the mass are grounded. The pair of glass plates form the parasitic capacitances C_{p1} and C_{p2} between the gold electrodes and the grounded test-mass. These parasitic capacitances are shown in Fig. 1 and originally result in a frequency mismatch between the LC resonators. The tuning capacitors C_v were used to compensate the associated frequency mismatch between the resonators.

Data availability: The datasets generated during and/or analyzed during the current study are available in the Zenodo repository https://doi.org/10.5281/zenodo.6397748

Code availability: The Matlab code which has been used for the evaluation of Allan deviation is available at https://www.mathworks.com/help/nav/ref/allanvar.html

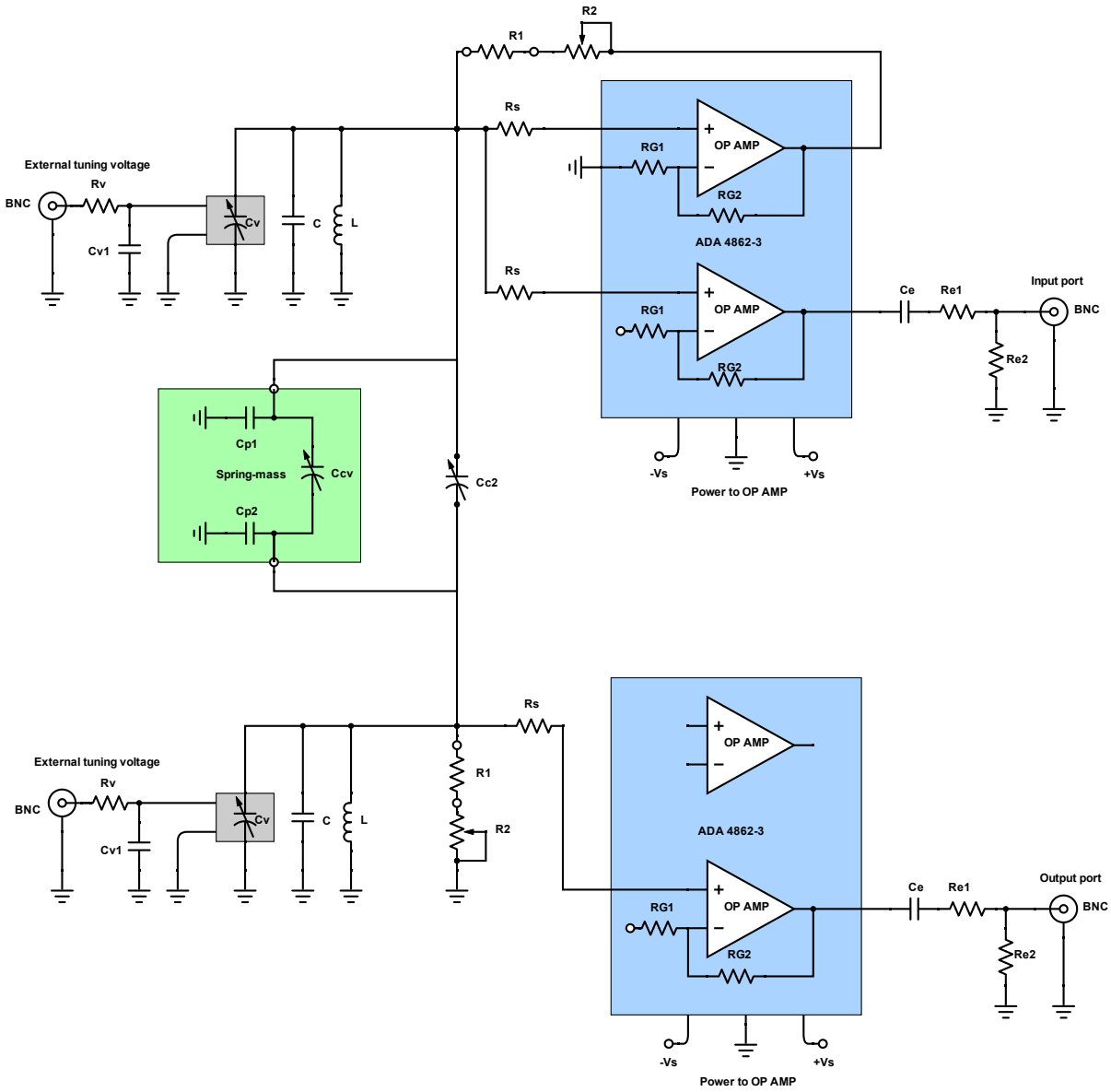

Extended Data Figure 1: **Schematic of the circuit diagram**. The blue elements are ADA4862- 3 amplifiers, while the green element indicates the spring-mass which provides the acceleration dependent capacitance C_{cv}.

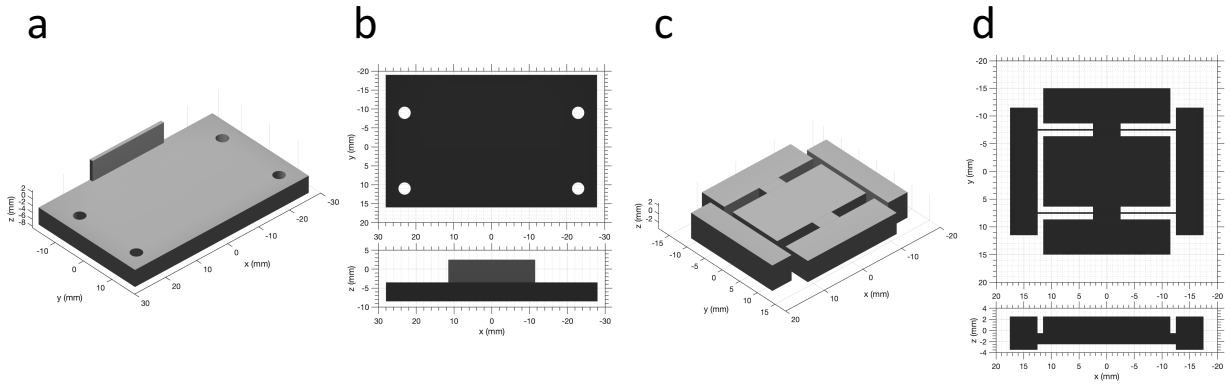

Extended Data Figure 2: **Details of the mechanical sensor elements**. **a,b,** Drawings of the copper platform. **c,d,** Drawings of the test-mass.

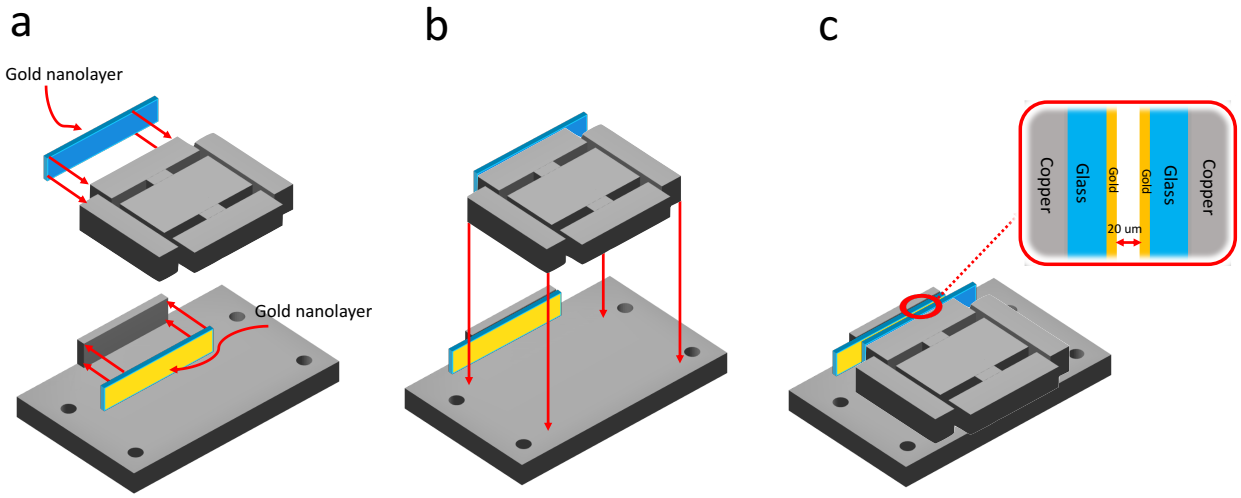

Extended Data Figure 3**: Assembly process of the acceleration capacitive sensor. a**, Deposition of the gold nanofilms on a glass substrate that create conductive electrodes which form the capacitors plates. Attachment of the glass plates to the stationary platform and test-mass. **b**, Placement of the test mass with glass plate on top of the copper base. **c**, Assembled capacitive inertial sensor. The inset shows the magnified view of the area between the capacitor plates which is about 20 um.